J. Fluid Mech. (1972), *vol.* 51, *part* 3, *pp.* 513–527
Printed in Great Britain

Nonlinear source-sink flow in a rotating pie-shaped basin

By GEORGE VERONIS AND C. C. YANG
Department of Geology and Geophysics, Yale University

(Received 5 May 1971)

Source-sink flows in a rotating pie-shaped basin provide a laboratory analogue of wind-driven ocean circulation (Stommel, Arons & Faller 1958). Experiments and theory are presented here for flows which are mildly nonlinear. Theory and experiment show satisfactory agreement for the intense flow in the western boundary-layer region which contains the strongest nonlinear effects. The strengths of the sources and sinks were increased in the experiments in an attempt to induce an instability in the western boundary layer. However, the western boundary layer was always stable, even for relatively large Rossby numbers. Photographs from experiments with a basin of semicircular cross-section show the difference between eastern and western boundary layers in a striking manner.

1. Introduction

Stommel *et al.* (1958) showed how the flow generated by sources and sinks in a rotating pie-shaped basin (figure 1) of homogeneous fluid with a free surface is analogous to wind-driven flows in the ocean. A subsequent study by Kuo & Veronis (1971) contained a systematic analysis of the boundary layers for the laboratory situation. It was shown in the latter paper that the parameters (rotation rate and length scales) for the laboratory study could be adjusted to simulate either Munk's (1950) lateral frictional model or Stommel's (1948) bottom friction model of wind-driven ocean circulation. Analyses for linear flow models showed satisfactory agreement between theory and experiment. The study is extended in the present paper to moderately nonlinear flows.

The next section includes a summary of the linear theoretical study and an extension of the analysis to nonlinear flows where the nonlinearity can be studied by conventional perturbation methods. The principal inertial effects are confined to the western boundary layer and the analysis is restricted to that region.

After a description of the experimental arrangement in §3, a comparison between theory and experiment is given in §4. The radial flow predicted by theory agrees satisfactorily with the observed flow. The discrepancy between theory and experiment is less than 8 %, even for relatively strong nonlinear flows where perturbation methods are not obviously valid. The largest discrepancies occur at low rotation rates where the boundary layers are quite thick and treating the individual boundary layers as isolated regions leads to substantial errors. For higher rotation rates the discrepancy is within the limits of observational error.

When the flow rate is increased, the flow pattern is altered. The western boundary-layer flow impinges on the rim boundary and a steady, stationary eddy is generated in the rim boundary layer (figure 10*a*, plate 2). The sinuous motion of the flow decays with distance along the rim.

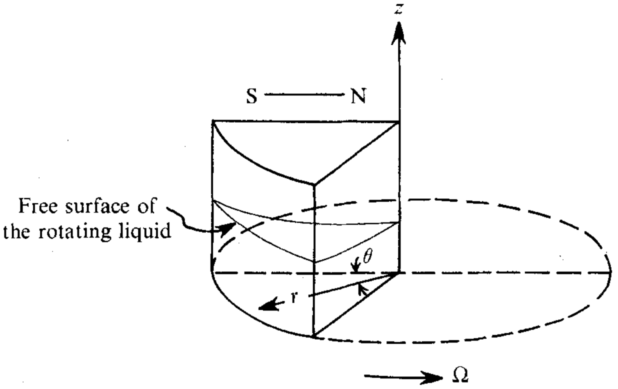

FIGURE 1. The configuration of a pie-shaped basin for the source-sink experiments. For counterclockwise rotation increasing *r* corresponds to southward direction.

Attempts to increase the flow rate to the point where the flow becomes unstable failed to produce an instability in the western boundary layer. Flows driven by a strong sink also proved to be stable. In the sink experiment none of the difficulties associated with eddy penetration from the source are present so that the flow is less affected by such extraneous effects. Since the Rossby number of the strong sink experiments approached unity, it seems likely that the flow in the western boundary layer is extremely stable.

Experiments with a large tank of semicircular cross-section exhibit the difference between eastern and western boundary layers in a striking manner. Figures 11 (*a*) and 11 (*b*) (plate 3) show the respective flow patterns for counterclockwise and clockwise rotation when the flow is mildly nonlinear. Qualitative features of the flow are discussed in § 5.

2. Theoretical analysis

Equations describing the steady fluid flow are obtained from the Navier–Stokes equations for a rotating fluid and the continuity equation. These equations in dimensionless form are

$$R\mathbf{v}.\nabla\mathbf{v} + 2\mathbf{k}\times\mathbf{v} = -\nabla p + E\nabla^2\mathbf{v}, \tag{1}$$

$$\nabla.\mathbf{v} = 0, \tag{2}$$

where $E(=\nu/\Omega a \leqslant 1)$ is the Ekman number, $R = (Q/A\Omega a E^{\frac{1}{2}} \leqslant 1)$ is the Rossby number, $\mathbf{k}$ is the unit vector in the z direction, $\mathbf{v}$ is the velocity vector with components (u, v, w) in the r, θ, z directions respectively, ν is the kinematic viscosity, a is the radius of the container, A is the horizontal area of the container, and Q

is the rate of volume influx. The centrifugal and gravitational body force terms are absorbed in p.

The boundary conditions are $\mathbf{v} = 0$ at all solid surfaces. The free-surface condition is

$$w = \dot{\zeta} + Fru + FR\left[u\frac{\partial\zeta}{\partial r} + \frac{v}{r}\frac{\partial\zeta}{\partial R}\right] \tag{3}$$

at the free surface $z = h(r) + \zeta(r, \theta, t)$, $[\zeta \ll h]$, where $h(r)$ is the shape of the paraboloidal free surface associated with the solid body rotation, ζ is a variation in height of the free surface due to the fluid flow, $\dot{\zeta} \equiv \partial\zeta/\partial t$, and $F(= \Omega^2 a/g)$ is the Froude number. The order of magnitude of $\dot{\zeta}$ is taken to be $E^{\frac{1}{2}}$.

We take $R = \gamma E^{\frac{1}{2}}$, where γ is a constant smaller than one. This restriction allows us to treat the nonlinear terms by perturbation methods.

Rather than proceeding formally at this stage, we prefer to make use of established results from linear rotating fluid theory to motivate the procedure. The variables will be separated into interior contributions (denoted by subscript I), side-wall boundary-layer contributions (denoted by subscript s) and Ekman boundary-layer contributions. It is well known from Ekman layer theory (Greenspan 1968) that if u_I and/or v_I are $O(1)$ then w_I is $O(E^{\frac{1}{2}})$. Similarly if u_s is $O(1)$ w_s is $O(E^{\frac{1}{4}})$.

The usual procedure is to expand the interior variables in powers of $E^{\frac{1}{2}}$. Thus

$$(\mathbf{v}_I, p_I) = (\mathbf{v}_0, p_0) + E^{\frac{1}{2}}(\mathbf{v}_1, p_1) + \ldots, \tag{4}$$

where $w_0 \equiv 0$ as noted above. The lowest order interior equations describe geostrophic balance. Therefore, the terms multiplied by $R(= \gamma E^{\frac{1}{2}})$ in (3) vanish at lowest order and (3) becomes

$$w_I = \dot{\zeta} + Fru_I \quad \text{at} \quad z = h. \tag{5}$$

The condition that the bottom Ekman layer imposes on the interior vertical velocity is

$$w_I = \frac{E^{\frac{1}{2}}}{2}\left[\frac{1}{r}\frac{\partial}{\partial r}(rv_I) - \frac{1}{r}\frac{\partial}{\partial\theta}u_I\right] \quad \text{at} \quad z = 0. \tag{6}$$

We have already noted that w_I is at most $O(E^{\frac{1}{2}})$. If $F > O(E^{\frac{1}{2}})$ then, from (5), $u_I < O(E^0)$. In this case the left side of (5) can be neglected and

$$u_I = -\dot{\zeta}/rF \tag{7}$$

throughout the interior region since u_I is independent of z. Equation (7) describes the interior radial velocity for the linear problem. It is also valid for the nonlinear problem, as long as $F > O(E^{\frac{1}{2}})$ for the flow under consideration. The nonlinear contribution enters via the side-wall boundary layer.

The linear $E^{\frac{1}{4}}$ layers

The linear equations for the $E^{\frac{1}{4}}$ side-wall boundary layers near $\theta = 0$ and $\theta = \theta_0$ are

$$\left.\begin{aligned} 2v_s &= \frac{\partial p_s}{\partial r} - \frac{E}{r^2}\frac{\partial^2 u_s}{\partial\theta^2}, \\ 2u_s &= -\frac{1}{r}\frac{\partial p_s}{\partial\theta}, \quad 0 = \frac{\partial p_s}{\partial z}, \\ \frac{1}{r}\frac{\partial}{\partial r}(ru_s) &+ \frac{1}{r}\frac{\partial v_s}{\partial\theta} + \frac{\partial w_s}{\partial z} = 0, \end{aligned}\right\} \tag{8}$$

where $u_s = u_{s0}+E^{\frac{1}{4}}u_{s1}$, $v_s = E^{\frac{1}{4}}v_{s0}+E^{\frac{1}{2}}v_{s1}$, $p_s = E^{\frac{1}{4}}p_{s0}+E^{\frac{1}{2}}p_{s1}$, $w_s = E^{\frac{1}{4}}w_{s0}$. The system is closed when subscript 1 variables are taken into account. The free-surface condition (3) for this layer is

$$w_s = Fru_s. \tag{9}$$

As shown by Kuo & Veronis (1971), if equations (8) together with condition (9) and the Ekman layer condition (6) are written to $O(E^{\frac{1}{4}})$ and all variables except p_{s0} are eliminated, the following equation must be solved:

$$\frac{1}{r^4}\frac{\partial^4 p_{s0}}{\partial\theta^4}-\frac{1}{r^2hE^{\frac{1}{2}}}\frac{\partial^2 p_{s0}}{\partial\theta^2}-\frac{2F}{hE}\frac{\partial p_{s0}}{\partial\theta} = 0. \tag{10}$$

Here, the θ variation is $O(E^{-\frac{1}{4}})$. The boundary conditions near $\theta = 0$ and $\theta = \theta_0$ for the problem are

$$u_s+u_I = 0, \quad v_s+v_I = 0,$$

or in terms of pressure

$$\frac{1}{r}\frac{\partial p_s}{\partial\theta}+\frac{1}{r}\frac{\partial p_I}{\partial\theta} = 0, \quad \frac{\partial p_s}{\partial r}+\frac{\partial p_I}{\partial r} = 0. \tag{11}$$

The linear solution for the pressure in the interior plus the side-wall boundary layers is (to $O(E^{\frac{1}{4}})$)

$$\begin{aligned} p = (2\dot{\zeta}/F)\{\theta-\theta_0+(E^{\frac{1}{4}}/r\alpha_3)+E^{\frac{1}{4}}\,[c_1\exp\left(-\alpha_1 r\theta E^{-\frac{1}{4}}\right) \\ +c_2\exp\left(-\alpha_2 r\theta E^{-\frac{1}{4}}\right)+c_3\exp\left(\alpha_3 r(\theta-\theta_0)\,E^{-\frac{1}{4}}\right)]\}, \end{aligned} \tag{12}$$

where

$$\left.\begin{aligned} c_1 &= [1/(\alpha_1-\alpha_2)\,r]\,[1-\alpha_2 rE^{-\frac{1}{4}}(\theta_0-E^{\frac{1}{4}}/r\alpha_3)], \\ c_2 &= [1/(\alpha_2-\alpha_1)\,r]\,[1-\alpha_1 rE^{-\frac{1}{4}}(\theta_0-E^{\frac{1}{4}}/r\alpha_3)], \\ c_3 &= -1/\alpha_3 r, \end{aligned}\right\} \tag{13}$$

α_1, α_2 are the roots having positive real part of the cubic equation

$$\alpha^3-(1/h)\,\alpha+2Fr/hE^{\frac{1}{4}} = 0 \tag{14}$$

and α_3 is the root with positive real part of the cubic equation

$$\alpha^3-(1/h)\,\alpha-2Fr/hE^{\frac{1}{4}} = 0. \tag{15}$$

For the experimental conditions described later α_1 and α_2 are real for small r and complex conjugates for r near 1.

Nonlinear $E^{\frac{1}{4}}$ layers

The nonlinear terms are treated by a perturbation procedure. Let

$$\phi = \phi^0+\gamma\phi^1+\gamma^2\phi^2+\ldots, \tag{16}$$

where ϕ is any of the dependent variables and the superscript on ϕ corresponds to the order in γ. The set with superscript 0 is the linear system summarized above. The first-order system in γ of the Navier–Stokes equation is given by

$$\left.\begin{aligned} u^0\frac{\partial u^0}{\partial r}+\frac{v^0}{r}\frac{\partial u^0}{\partial\theta}-\frac{v^0v^0}{r}-2v^1 &= -\frac{\partial p^1}{\partial r}+E\nabla^2u^0, \\ u^0\frac{\partial v^0}{\partial r}+\frac{v^0}{r}\frac{\partial v^0}{\partial\theta}+\frac{u^0v^0}{r}+2u^1 &= -\frac{1}{r}\frac{\partial p^1}{\partial\theta}+E\nabla^2v^0, \\ u^0\frac{\partial w^0}{\partial r}+\frac{v^0}{r}\frac{\partial w^0}{\partial\theta} &= -\frac{\partial p^1}{\partial z}+E\nabla^2w^0. \end{aligned}\right\} \tag{17}$$

It was pointed out earlier that (7) describes the interior flow even in the nonlinear case for the situation treated here. Therefore, it is necessary to take the nonlinear terms into account only in the side-wall boundary layers. Furthermore, from the orders of magnitude established for the interior and the $E^{\frac{1}{4}}$ layer solutions it can be shown that the lowest order nonlinear effects enter only through the interactions of the contributions from the side-wall layers themselves. The product terms involving interior variables times boundary-layer variables do not contribute to lowest order. *Hence the system* (17) *can be written with subscripts* s *on all of the variables*. Dropping negligible terms we arrive at the set

$$\left.\begin{aligned} u_s^0\frac{\partial u_s^0}{\partial r}+\frac{v_s^0}{r}\frac{\partial u_s^0}{\partial \theta}-2v_s^1 &= -\frac{\partial p_s^1}{\partial r}+\frac{E}{r^2}\frac{\partial^2 u_s^1}{\partial \theta^2},\\ 2u_s^1 = -(1/r)\,\partial p_s^1/\partial\theta, &\quad \partial p_s^1/\partial z = 0.\end{aligned}\right\} \tag{18}$$

The boundary conditions at the bottom and at the free surface are to lowest order

$$\left.\begin{aligned} w_s^1 &= (E^{\frac{1}{2}}/4r^2)\,\partial^2 p_s^1/\partial\theta^2 \quad \text{at} \quad z=0,\\ w_s^1 &= -\tfrac{1}{2}F\,\partial p_s^1/\partial\theta \quad \text{at} \quad z=h.\end{aligned}\right\} \tag{19}$$

We proceed as for the linear problem and expand each of the variables in powers of $E^{\frac{1}{4}}$. The only difference between the present set (18) and the linear set (8) is in the inhomogeneous terms with superscript 0. Hence, the problem reduces to solving

$$\frac{1}{r^4}\frac{\partial^4 p_{s0}^1}{\partial\theta^4}-\frac{1}{r^2hE^{\frac{1}{2}}}\frac{\partial^2 p_{s0}^1}{\partial\theta^2}-\frac{2F}{hE}\frac{\partial p_{s0}^1}{\partial\theta}+\frac{2}{r}\frac{\partial}{\partial\theta}\left[u_s^0\frac{\partial u_s^0}{\partial r}+\frac{v_s^0}{r}\frac{\partial u_s^0}{\partial\theta}\right]=0, \tag{20}$$

where the superscript 0 terms are known. Equation (20) can be integrated with respect to θ to yield

$$\frac{1}{r^3}\frac{\partial^3 p_{s0}^1}{\partial\theta^3}-\frac{1}{rhE^{\frac{1}{2}}}\frac{\partial p_{s0}^1}{\partial\theta}-\frac{2Fr}{Eh}p_{s0}^1+2\left[u_s^0\frac{\partial u_s^0}{\partial r}+\frac{v_s^0}{r}\frac{\partial u_s^0}{\partial\theta}\right]=0. \tag{21}$$

(The arbitrary function of r and z which results from the integration must vanish because all of the subscripts s variables and their derivatives vanish with increasing distance from the boundary.)

The principal contribution of the nonlinear terms is from the boundary layer near $\theta = 0$, where u_s is large. The contribution from the boundary layer near $\theta = \theta_0$ is no larger than the nonlinear contribution in the interior, which is negligible at this order. Hence we restrict our discussion to the boundary layer near $\theta = 0$ (the 'western' boundary layer) which satisfies the condition that the velocity vanishes at $\theta = 0$. The interior solution of the superscript 1 variable is taken to satisfy the condition that the normal velocity v vanishes at $\theta = \theta_0$.

The form of the solution of (21) near $\theta = 0$ depends on whether the roots α_1, α_2, α_3 of (14) and (15) are real or complex. When the roots are real, the solution is

$$\begin{aligned} p_{s0}^1 = c_4\exp[-\alpha_1\psi]+c_5\exp[-\alpha_2\psi]+c_6\exp[-2\alpha_1\psi]&\\ +c_7\exp[-2\alpha_2\psi]+[c_8+c_9\theta E^{-\frac{1}{4}}]\exp[-(\alpha_1+\alpha_2)\psi],& \end{aligned} \tag{22}$$

where $\psi = r\theta E^{-\frac{1}{4}}$ and

$$\left.\begin{aligned}
c_4 &= -[c_6(2\alpha_1-\alpha_2)+c_7\alpha_2+c_8\alpha_1-c_9/r]/(\alpha_1-\alpha_2),\\
c_5 &= [c_6\alpha_1-c_7(\alpha_1-2\alpha_2)+c_8\alpha_2-c_9/r]/(\alpha_1-\alpha_2),\\
c_6 &= c_1^2\alpha_1\alpha_1'/(12\alpha_1/h-28Fr/hE^{\frac{1}{4}}),\\
c_7 &= c_2^2\alpha_2\alpha_2'/(12\alpha_2/h-28Fr/hE^{\frac{1}{4}}),\\
c_8 &= [c_1c_2(\alpha_1\alpha_2)'-(\alpha_1-\alpha_2)(\alpha_1c_1c_2'-\alpha_2c_2c_1')]/[6\alpha_1a_2(\alpha_1+\alpha_2)\\
&\quad -4Fr/hE^{\frac{1}{4}}]+(C_9/r)[3(\alpha_1+\alpha_2)^2-1/h]/[3\alpha_1\alpha_2(\alpha_1\alpha_2)-2Fr/hE^{\frac{1}{4}}],\\
c_9 &= rc_1c_2(\alpha_1-\alpha_2)[\alpha_1\alpha_2'-\alpha_2\alpha_1']/[6\alpha_1\alpha_2(\alpha_1+\alpha_2)-4Fr/hE^{\frac{1}{4}}],
\end{aligned}\right\} \tag{23}$$

and primes denote d/dr.

When the roots α_1 and α_2 are complex conjugates with $\alpha_1 = a+bi$ then $c_1(r)$ and $c_2(r)$ are also complex conjugates and $c_1 = d+fi$. In this case the solution is algebraically much more complicated. Its form is

$$\begin{aligned}
p_{s0}^1 = c_4\exp[-\alpha_1,\psi]+c_5\exp[-\alpha_2\psi]+\exp[-2a\psi]\{c_6[\mathrm{Re}\,(c_1e^{-ib\psi})]^2\\
+c_7[\mathrm{Im}(c_1e^{-ib\psi})]^2+c_8[\mathrm{Re}\,(c_1e^{-ib\psi})][\mathrm{Im}\,(c_1e^{-ib\psi})]+c_9+c_{10}\theta E^{-\frac{1}{4}}\},
\end{aligned} \tag{24}$$

where $\psi = r\theta E^{-\frac{1}{4}}$

and

$$\left.\begin{aligned}
c_4(\alpha_1,\alpha_2) &= (\alpha_2/(\alpha_1-\alpha_2))(d^2c_6+f^2c_7+dfc_8+c_9)+(1/(\alpha_1-\alpha_2))\{-2ac_9+c_{10}/r\\
&\qquad -2c_6d(da-fb)-2fc_7(db+fa)-c_8[b(d^2-f^2)+2dfa]\},\\
c_5(\alpha_1,\alpha_2) &= c_4(\alpha_2,\alpha_1),\\
c_7 &= -(1/D)\{[2bb'G+(ab)'K]H+(aa'+bb')K^2+24ab^2(aa'+bb')G\},\\
c_6 &= -c_7-(2/D)(aa'+bb')G^2-2(aa'+bb')K^2,\\
c_8 &= (H/D)\{2(ab)'G+2(aa'-bb')K\},\\
c_9 &= -(2b/H)\{d(bd'-af')+f(ad'+bf')\}-(c_{10}/rH)(12a^2-1/h),\\
c_{10} &= -(2r/H)(d^2+f^2)b(ab'-ba'),\\
G &= -8a^3+24ab^2+2a/h-2Fr/hE^{\frac{1}{4}},\quad H = -8a^3+2a/h-2Fr/hE^{\frac{1}{4}},\\
D &= [G^2+K^2]H,\ K = 24a^2b-8b^3-2b/h,
\end{aligned}\right\} \tag{25}$$

and a prime denotes d/dr.

3. The experimental arrangement and method of observation

A metal turntable (90 cm diameter) which was driven by a synchronous motor through a variable speed Graham transmission and a geared timing belt and could be rotated at a uniform angular velocity accurate to about 0·1 % was used. The alignment of the rotational axis with the vertical was about 3 sec of arc under the condition of no load and better than 5 sec of arc under full load with a careful balance of the experimental apparatus mounted on the turntable.

A double (side) wall pie-shaped Plexiglas container of radius $a = 45$ cm, apex angle $\theta_0 = \frac{1}{3}\pi$ and height 25 cm was used for most of this study. The simplicity of the geometry facilitates theoretical descriptions and comparisons with experiment. The false wall eliminates the effect of room temperature fluctuations on the working fluid and the large radius minimizes overlapping of the different side-wall boundary layers. Containers of 45 cm radius with curved or sliced side-wall boundaries were also constructed for studying the influence of lateral boundaries on the fluid flow.

A double-tube (100 ml) syringe pump was used for injecting or withdrawing fluid into or from the test container. The pump mechanism consists of a threaded drive block travelling along a rotating screw shaft which contains 24 threads per inch. A variable speed Bodine d.c. motor (NSH-12R) provides constant pumping at various flow rates. The critical design requirement is a parallel motion of the threaded drive block and the two glass pumps. This can be easily achieved by machining a block with a metal base which accommodates syringes and the rotating screw shaft. Thus the centre-lines of each component are parallel and all moving parts move in one direction. Stop switches at the two ends of the pump terminate the pumping or sucking action.

Owing to the limitation of the available syringe size, for a higher influx rate ($Q > 1\,\mathrm{cm^3/sec}$) experiment such as the study of an unstable flow we relied on another method for infusing fluid into the container. The method is simply to drain working fluid down to the test container from a reservoir through a tube and stopcock. No air bubble is allowed in the passage between the reservoir and the test container. During the experiment, we maintained a constant water level at the reservoir by continuously supplying fluid from a stationary frame to the reservoir through a small funnel placed near the centre of the turntable.

All injections or withdrawals of the fluid were made at some corner of the container through a 0·4 cm. I.D. glass tube. A 35 mm motor-driven Nikon camera was mounted on a stationary frame vertically above the test container. In this way photographs could be taken once for every rotation of the table (sufficient for our purpose). The camera was actuated by a magnetic Reed switch and RC circuit. The advantage of the above arrangement is an increase of the stability of the rotating liquid,† but there is a minor difficulty in generating a sharp image because of relative motion of the object and the camera. To maximize the clarity, the camera shutter speed was shortened to 1/250 sec while the aperture was set (enlarged) to $f = 2$. One can further shorten the shutter speed by using a high-speed recording film.

For flow visualization we used a method described by Baker (1966). A pH indicator thymol blue solution (0·1 N) was used as the working fluid. The indicator, blue when basic and yellow to orange when acidic, was titrated to the end-point where it is slightly acidic. Electrode grids of 0·005 cm stainless steel wire were stretched horizontally across the container at various desired locations and 4 cm above the bottom. When a d.c. potential is applied across the grids, fluid around the positive electrode becomes locally basic and turns blue.

A sequence of these dye lines, produced at fixed intervals, was photographed (on Kodak Tri-X film) as they were swept off the electrode. The distance between

---

† Any weight mounted non-symmetrically on the turntable tends to introduce a variability in the rotation rate.

two successive dye segments was measured from the photographic record to compute the observed velocity (u, v). To improve the dye image for accurate velocity measurements the electrodes were painted (insulated) segment by segment. Thus one can easily identify the movement of each dashed dye line.

In this experiment our main concern was the intense 'western' boundary-layer flow. In the interior, the magnitude of fluid flow was one order or so less than the boundary-layer flow and was too small to be measured accurately. For velocities greater than 0·15 cm/sec the blue dye segment formed around the electrode was swept off so rapidly that the dye lines were not sharp enough for an accurate measurement. Hence, in this study experiments were restricted to those with a maximum velocity of 0·15 cm/sec.

During the course of the day, room temperature variations were less than 0·4 °C. To eliminate the influence of air flow on the working fluid the test container was covered with a clear flat Plexiglas plate. The experimental arrangement was set up several hours before the actual runs and the system was allowed to come to thermal equilibrium with the room temperature. The experimental procedure was similar for all studies. After the turntable had started rotating, a period (20 min say) was allowed for the working fluid to spin up. A test to check the uniform rotation of the fluid was first made by observing the movement of a dye line as a function of time. Then a source (sink) Q, preset at a desired value, was applied and after 1·5 to 7 min, depending on the strength of Q, the flow observations were made.

4. Experimental results and comparison with theory

After some preliminary experiments we determined the optimum experimental conditions which could produce a stable 'rigid body' rotation. (Under some conditions, e.g. imperfect vertical alignment of the axis of rotation, a very weak circulation along the side wall of the container can occur when the rotating liquid has a free surface.) In the present study the experiments were conducted at rotation rate of $\Omega = 1{\cdot}0$ rad/sec ($E = 4{\cdot}94 \times 10^{-6}$, $F = 4{\cdot}59 \times 10^{-2}$) and $\Omega = 1{\cdot}83$ rad/sec ($E = 2{\cdot}7 \times 10^{-6}$, $F = 1{\cdot}53 \times 10^{-1}$) with a static water height h_0 of 8 to 9 cm. Photographic records of a weak drifting as a function of time were taken before each experiment and used as a reference for the velocity measurements in the experiment. The source (sink) strength Q was between 0·045 cm^3/sec and 0·9 cm^3/sec, so that the nonlinear factor $\gamma\,(= R/E^{\frac{1}{2}} = (Q/A)(a/\nu))$ was between 0·2 and 3·8. In the theoretical analysis we considered γ to be smaller than unity. However, experimental results for $\gamma > 1$ are also compared with the perturbation analysis outlined in §2.

As mentioned in §2, one can obtain real or complex numbers for α_1 and α_2 depending on the values of Ω, r and a. When the slope $(= Fr = \Omega^2 ar/g$)of the paraboloidal free surface of the rotating fluid is large, the values of α_1 and α_2 become complex. The slope of the surface was large in this sense near the outer rim and small near $r = 0$. In this study, velocities were measured on the 'western' side of a pie-shaped basin at distance of $r \simeq 15$ cm and $r \simeq 30$ cm from the apex of the container. For $\Omega = 1{\cdot}0$ rad/sec, α_1 and α_2 are real numbers when $r = 15$ cm

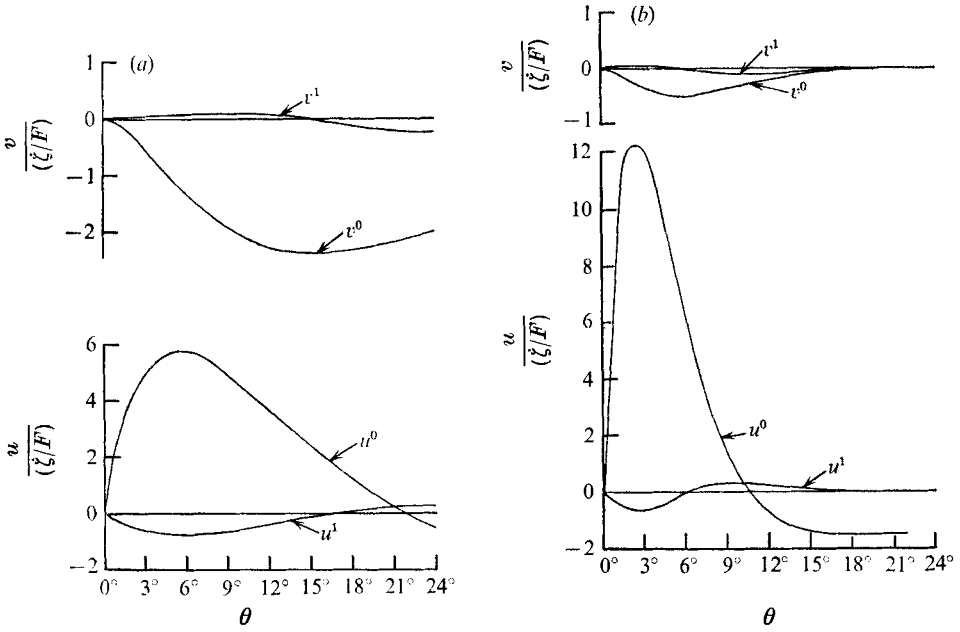

FIGURE 2. Normalized dimensionless velocity profile. Physical constants: $\Omega = 1$ rad sec, $h_0 = 8$ cm; (*a*) $r = 15{\cdot}4$ cm; (*b*) $r = 30{\cdot}6$ cm.

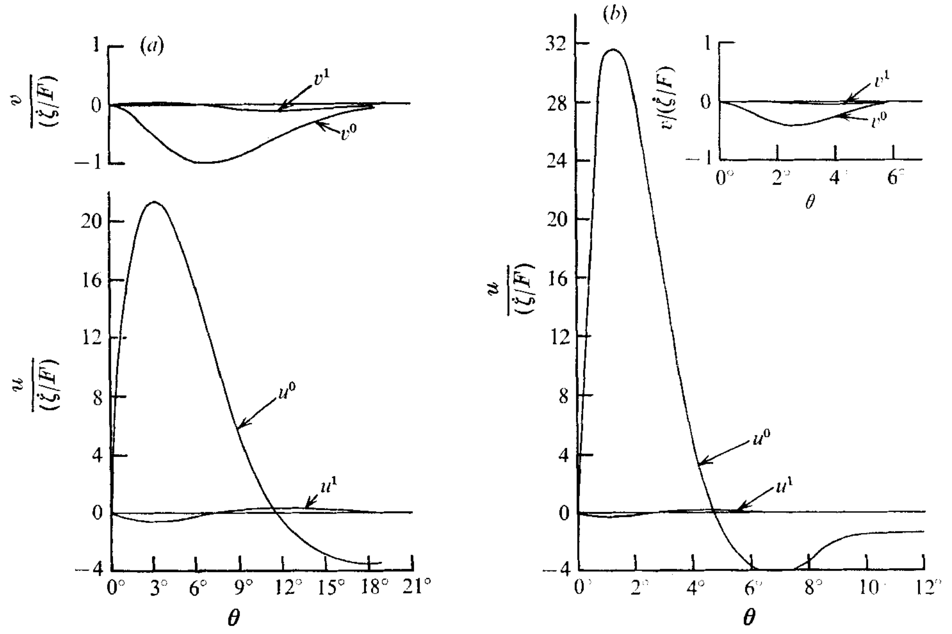

FIGURE 3. Normalized dimensionless velocity profile. Physical constants: $\Omega = 1{\cdot}83$ rad/sec, $h_0 = 8$ cm; (*a*) $r = 15{\cdot}08$ cm; (*b*) $r = 30{\cdot}6$ cm.

and complex conjugate when $r = 30$ cm; for $\Omega = 1{\cdot}83$ rad/sec, both locations give complex conjugate roots.

The normalized dimensionless velocity profiles $u/(\dot{\zeta}/F)$, $v/(\dot{\zeta}/F)$ computed from (12), (22), (24) with the above physical conditions are shown in figures 2 and 3.

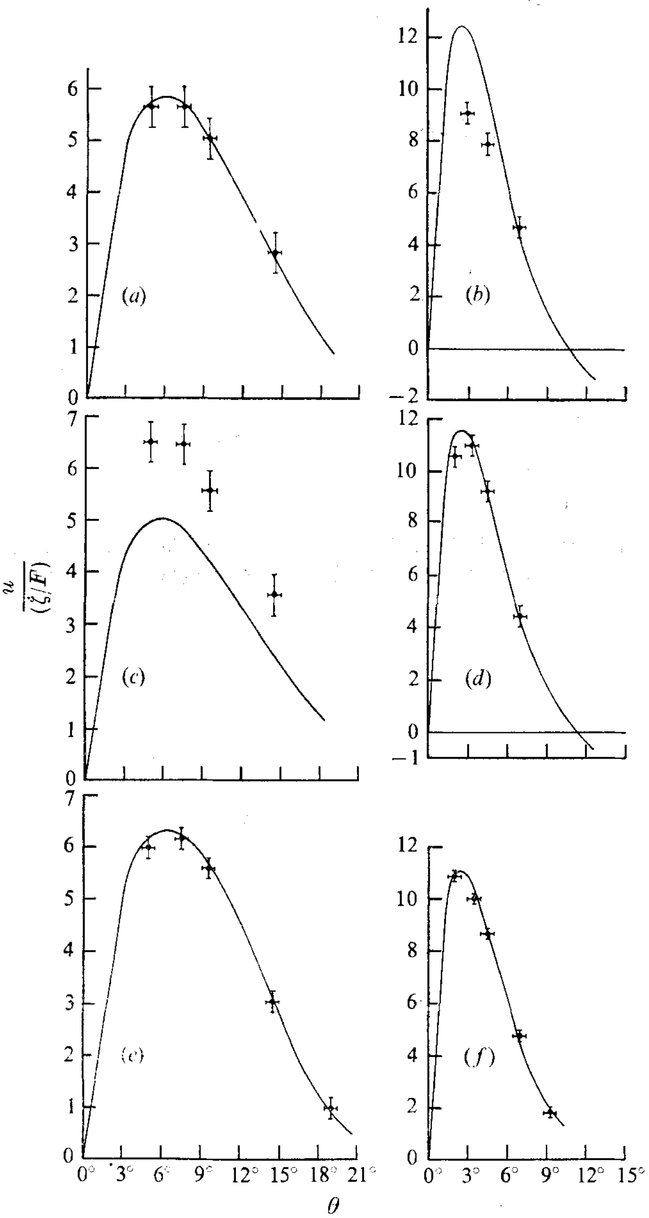

FIGURE 4. Comparison of theory and experimental data for u. Rotation rate $\Omega = 1$ rad/sec; ———, theory; +, experiment, showing scale of measurement error.

	(a)	(b)	(c)	(d)	(e)	(f)
	Sink flow	Sink flow	Source flow	Source flow	Sink flow	Source flow
γ	0·645	0·645	0·645	0·645	1·89	1·89
$r(\approx)$	$\frac{1}{3}$	$\frac{2}{3}$	$\frac{1}{3}$	$\frac{2}{3}$	$\frac{1}{3}$	$\frac{2}{3}$

From these figures one can see that for a higher rotation rate, i.e. smaller E, the boundary-layer jet v^0 has narrower width and higher radial velocity and the nonlinear contribution is small. Similarly for a given rotation rate the boundary-layer width is smaller at larger radii where the slope of the free surface is larger. The above velocity profiles are plotted for the case where fluid is injected into the container (source flow). In the reverse case (sink flow) the signs of u^0 and v^0 are changed but u^1 and v^1 keep the same sign. Consequently, in the source experiment the nonlinear contribution of u^1 retards the main flow u^0 and widens the jet. The reverse situation holds in the sink experiment. In figure 4 the (Lagrangian) radial velocities measured from photographic records are compared with the theoretically calculated (Eulerian) velocities near the western wall for $\Omega = 1$ rad/sec and for various values of γ (i.e. Q). Figure 4(a) shows very good agreement between theoretical and experimental values of the velocity at $r \simeq \frac{1}{3}$ for sink flow. The agreement is much poorer for the same comparison (figure 4(b)) at $r \simeq \frac{2}{3}$. On the other hand source flow at $r \simeq \frac{1}{3}$ (figure 4(c)) shows poor agreement, whereas at $r \simeq \frac{2}{3}$ (figure 4(d)) the two results compare very well. These discrepancies are due to the fact that the different boundary layers for this rotation rate are relatively thick and tend to overlap, thus decreasing the validity of the boundary-layer calculations; e.g. the rim boundary layer has a thickness of about one-third the radius near the western wall. For the case of a sink the boundary-layer flow is from the outer rim toward the apex and the rim boundary layer contributes significantly to the distortion. When a source drives the flow, the boundary-layer flow is from the apex to the rim and the western boundary layer is relatively unaffected by the rim boundary layer. The boundary layer near the apex has more effect on the results near the wall at $r = \frac{1}{3}$ when the flow is from the apex to rim (source flow) than when it is from rim to apex (sink flow).

Substantially better agreement is shown in figures 5(a)–(e), where the rotation rate is higher ($\Omega = 1{\cdot}83$ rad/sec) and the boundary layers are considerably thinner so that the boundary-layer overlap which contributed to the discrepancies in figure 4 is absent. The figures compare theory and experiment for linear ($\gamma = 0{\cdot}63$), moderately nonlinear ($\gamma = 1{\cdot}89$) and strongly nonlinear ($\gamma = 3{\cdot}78$) cases. Even in the latter case, where perturbation theory is not applicable *a priori*, the comparison gives excellent agreement.

The azimuthal velocity near the side walls is more difficult to measure because the flow is relatively weak. Figure 6 compares v at $r = \frac{1}{3}$, for theory and experiment, for the case of slow rotation ($\Omega = 1$ rad/sec) and for both source and sink flow. The agreement is quite good, particularly when one considers the magnitude of observational error.

Observed flow patterns for source and sink flows which were used for measuring the experimental results are shown in figure 7 (plate 1) for the case $\Omega = 1$ rad/sec, $\gamma = 0{\cdot}645$ and in figure 8 (plate 1) for $\Omega = 1$ rad/sec, $\gamma = 1{\cdot}89$. In the latter set of photographs the radially directed flow in the interior, outside the boundary layers, is clearly shown. One can also see that the boundary layers are quite thick for this rotation rate. Typical patterns with $\Omega = 1{\cdot}83$ rad/sec and $\gamma = 3{\cdot}78$ are shown in figure 9 (plate 2). The boundary layers are confined to narrower regions and the flow is much more intense. The flow near the apex in these experiments is strongly affected by the sharp angle ($\frac{1}{3}\pi$) at the apex, by the source or sink itself and by the lateral divergence or convergence where the slow flow along the eastern boundary meets the faster flow along the western wall. These effects all influence the measurements near $r = \frac{1}{3}$ and lead to discrepancies between theory and experiment.

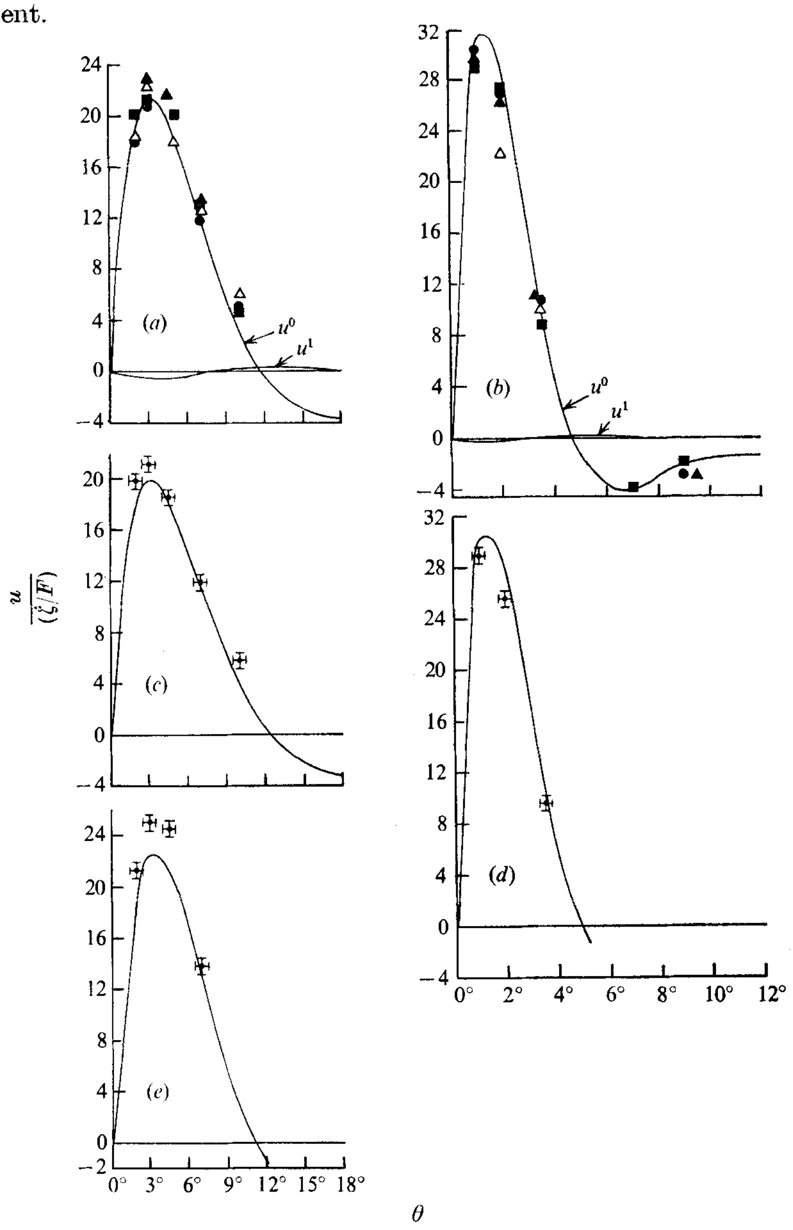

FIGURE 5. Comparison of theory and experimental data for u. Rotation rate $\Omega = 1{\cdot}83$ rad/sec; ——, theory; ○, experiment. In (*a*) and (*b*): no correction of the u^0 profile is made owing to small nonlinear contribution; ●, source flow, $\gamma = 1{\cdot}89$; ■, sink, $\gamma = 1{\cdot}89$; △, source, $\gamma = 0{\cdot}63$; ▲, sink, $\gamma = 0{\cdot}63$. $r \approx \frac{1}{3}, \frac{2}{3}$ for (*a*) and (*b*) respectively. For (*c*), (*d*) and (*e*), $\gamma = 3{\cdot}78$; (*c*) sink flow, $r \approx \frac{1}{3}$; (*d*) source, $r \approx \frac{2}{3}$; (*e*) sink, $r \approx \frac{1}{3}$.

Other sources of experimental error are: (i) Small drifting and horizontal oscillation of the neutrally buoyant dye marker in the rotating liquid due to the imperfection of the table drive. (An error of 1 mm in the measured dye position is significant for the results.) Such error was minimized by taking more photographic records and measurements as well as some reference photographs of weak drifting as mentioned earlier. (ii) Slight uncertainty in time measurement because a finite period (2·5 sec) is needed to generate the dye marker while it is being swept off the electrode during the course of the experiment. (iii) Viscous drag of the electrode wire on the flow. (iv) Slow thermal flows due to temperature difference between the working fluid and the air in the laboratory. Care was taken to minimize the thermal effects by using a tank with a false (side) wall for insulation.

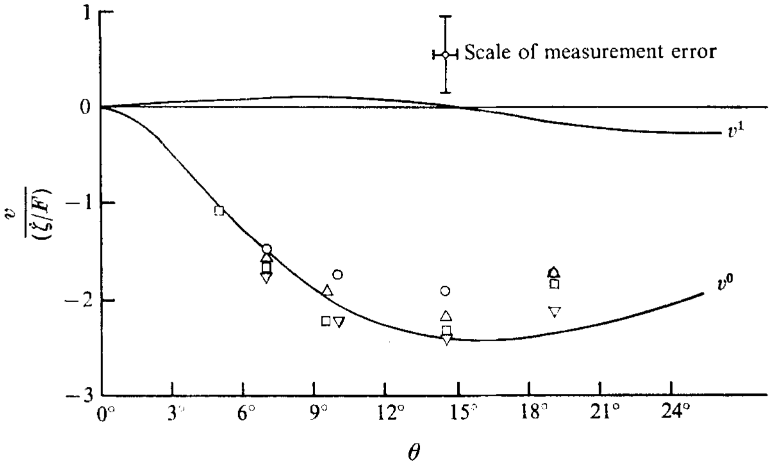

FIGURE 6. Comparison of theory and experimental data for v^0 at $r = \frac{1}{2}$. Rotation rate $\Omega = 1$ rad/sec; $\gamma = 0{\cdot}645$; ——, theory. Experimental data: ▽, ○, source flow; △, □, sink flow. No correction of the v^0 profile is made owing to small nonlinear contribution.

In this study, as mentioned earlier, experiments were restricted to cases with a maximum velocity of 0·15 cm/sec for an accurate measurement. As a result, the maximum value of γ was restricted to about 4 in our experiments for actual velocity measurements.

5. Additional experimental results

When the flow rate Q at the apex is increased, the flow can presumably become unstable. A preliminary experimental study of flow generated by a more intense source was made and a photograph of the flow for one of the experiments is shown in figure 10(*a*) (plate 2). The figure is a photograph of the flow pattern due to a source which was generated by a gravity-feed of fluid from a container above the tank. The parameters in this case are

$$\Omega = 1{\cdot}9\,\text{rad/sec}, \quad h_0 = 8{\cdot}3\,\text{cm}\,(E = 2{\cdot}6\times10^{-6}), \quad \gamma = 8{\cdot}1.$$

The dye lines were produced by continuous passage of current through the electrodes. Small-scale eddy-like motions are evident close to the western wall near

$r = \frac{1}{3}$. These eddies decay in increasing r because the flow is in fact stable and the eddies are due to disturbances introduced through the source at the apex. The analogous experiment with a source near the western rim is shown in figure 10 (*b*) (plate 2). The flow is steady. Even with much stronger sources no instability was detected in the western boundary layer.

The wave-like motion near the rim in figure 10 (*a*) has a steady fixed pattern in time. The western boundary jet impinges on the rim at the corner and the wavy boundary layer is generated as a result. The sinuous character of the flow near the rim decays with increasing azimuthal angle.

Analogous sink-flow experiments have the advantage that the disturbance from the sink does not interfere with the main flow in any obvious fashion. Even for experiments with $\gamma \sim E^{-\frac{1}{2}}$ (i.e. $R \sim 1$) the western boundary layer for the sink experiments was always stable.

Because of the overlapping of boundary layers for slower rotation rates in the pie-shaped basin we constructed a tank with a semicircular cross-section in order to isolate the boundary layers. Such a tank has the added advantage of exhibiting the difference in behaviour between the flows along eastern and western boundaries in a striking manner.

The tank has a radius of 40 cm and the mean fluid depth was 8·2 cm for the experiments which are reported. In figure 11 (*a*) (plate 3) the flow pattern is shown for the case where $\Omega = 1{\cdot}9$ rad/sec and $\gamma = 1{\cdot}328$. The source in this experiment is at the corner where the western wall meets the rim. (A source at the midpoint of the diameter creates a large disturbance and distorts the flow pattern.) The western boundary-layer flow near the left half of the diameter boundary is intense. Flow near the eastern boundary is much weaker. Near $r = 0$ the flow has a large radial divergence parallel to the diameter and fluid is sucked into the boundary-layer region from the interior. This converging flow near the 'apex' is obvious in the present experiment and must also be present in the pie-shaped basin experiments, though there it is masked by the overlapping of eastern and western boundary layers. The rim boundary layer is very thick near the western wall and narrows as the azimuthal angle increases from 0 to π. The interior flow is again radial but some distortion near the south-east corner is present because the rim boundary-layer flow is fairly intense and creates an eddy when it meets the eastern wall. The eddy penetrates about a third of the distance into the tank.

An analogous situation for source flow with clockwise rotation ($\Omega = -1{\cdot}9$ rad/sec and $\gamma = 2{\cdot}065$) is shown in figure 11 (*b*) (plate 3). The eastern and western boundaries are now on the left and right of $r = 0$ on the diameter respectively. The flow is essentially the reverse of the one in figure 11 (*a*). The source is again at the south-western corner (the corner at the right) and the eddy generated by the intense flow from the source distorts the western boundary layer considerably. The distortion is more noticeable here because of the dye line generated close to the south-western corner.

We are grateful to the National Science Foundation for support through grants GA 1416 and GA 11410.

REFERENCES

BAKER, D. J. 1966 A technique for the precise measurement of small fluid velocities. *J. Fluid Mech.* **26**, 573.

GREENSPAN, H. P. 1968 *The Theory of Rotating Fluids.* Cambridge University Press.

KUO, H. H. & VERONIS, G. 1971 The source-sink flow in a rotating system and its oceanic analogy. *J. Fluid Mech.* **45**, 441.

MUNK, W. H. 1950 On the wind-driven ocean circulation. *J. Meteorol.* **7**, 79.

STOMMEL, H. 1948 The western intensification of wind-driven ocean currents. *Trans. Am. Geoph. Union*, **29**, 202.

STOMMEL, H., ARONS, A. B. & FALLER, A. J. 1958 Some examples of stationary planetary flows. *Tellus*, **10**, 179.

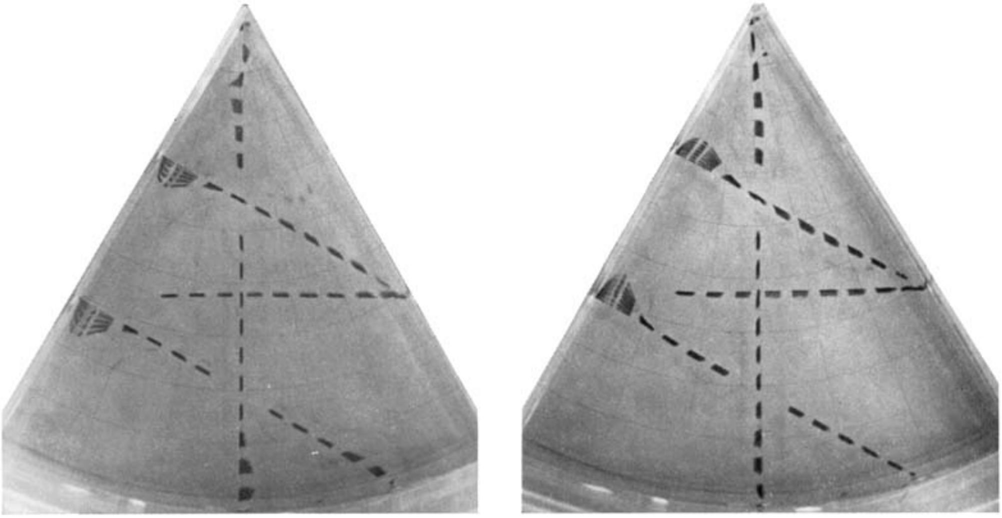
(*a*) (*b*)

FIGURE 7. The flow pattern of the source-sink experiment in a pie-shaped basin. Experimental conditions: $\Omega = 1$ rad/sec, $\gamma = 0{\cdot}645$, interval between dye pulses 18·9 sec, (*a*) source flow, (*b*) sink flow.

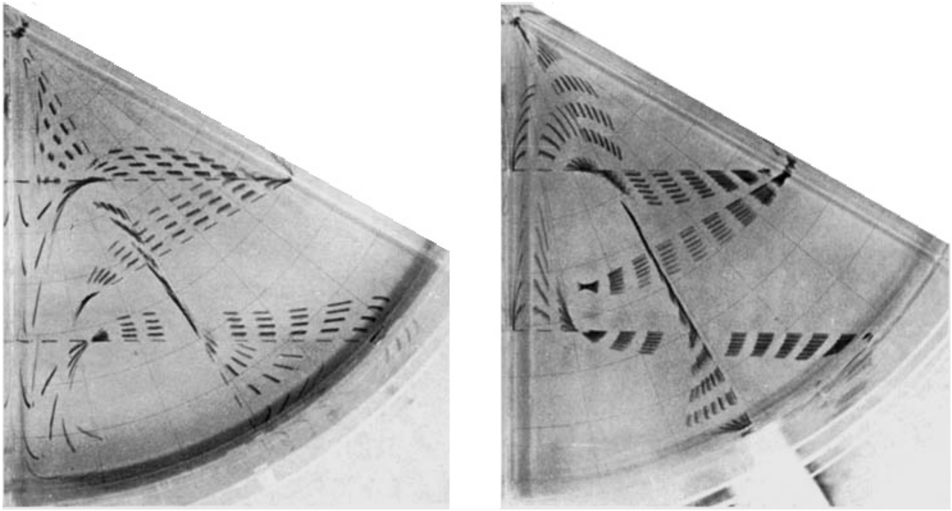
(*a*) (*b*)

FIGURE 8. The flow pattern of the source-sink experiment in a pie-shaped basin. Experimental conditions: $\Omega = 1$ rad/sec, $\gamma = 1{\cdot}89$. (*a*) Source flow, interval between dye pulses = 60 sec, (*b*) sink flow interval between dye pulses = 30 sec.

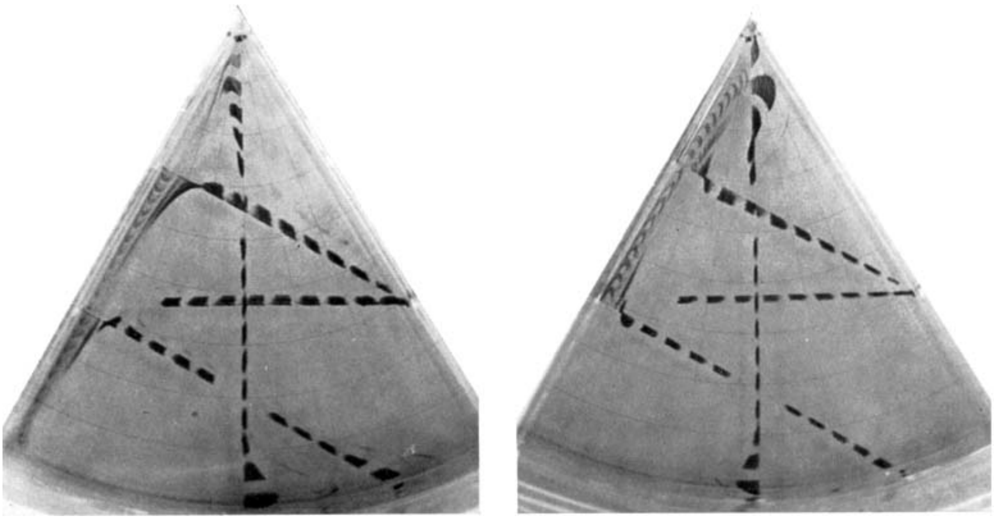

(*a*) (*b*)

FIGURE 9. The flow pattern of the source-sink experiment in a pie-shaped basin. Experimental conditions: $\Omega = 1{\cdot}83$ rad/sec, $\gamma = 3{\cdot}78$, interval between dye pulses = 6.88 sec, (*a*) source flow, (*b*) sink flow.

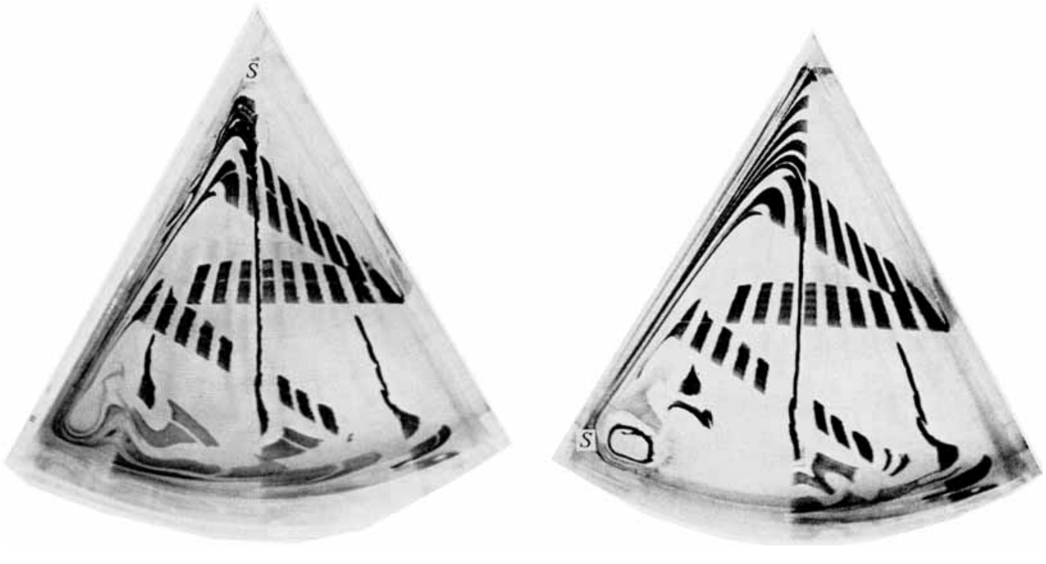

(*a*) (*b*)

FIGURE 10. The flow pattern with the source at the apex (*a*) and rim (*b*) in a pie-shaped basin. Experimental conditions: source flow, $\Omega = 1{\cdot}9$ rad/sec, $\gamma = 8{\cdot}1$. The photograph was taken 4·5 min after d.c. potential was applied across the electrode.

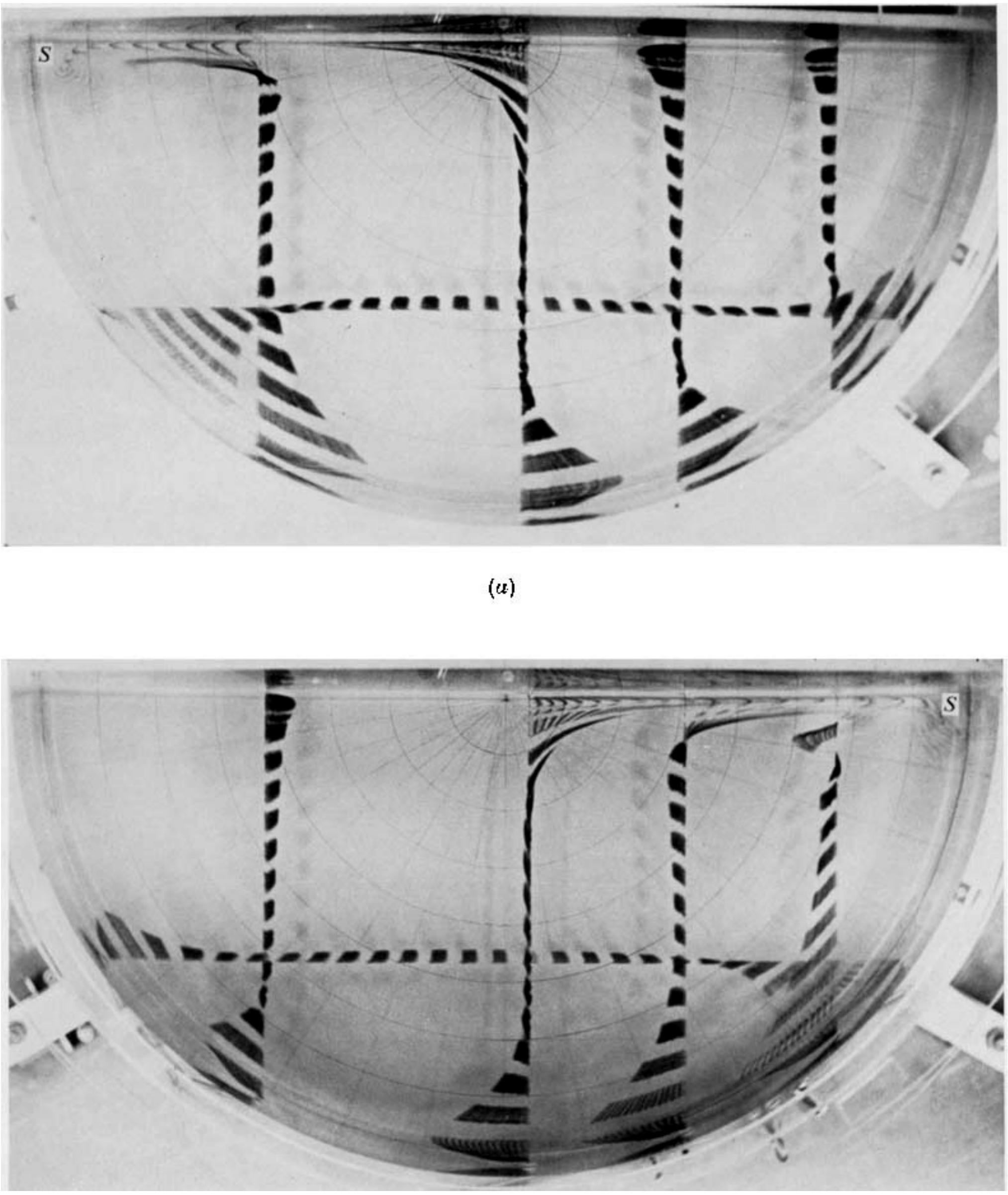

FIGURE 11. The flow pattern of the source-sink experiment in a semicircular basin. Experimental conditions: source flow, $\Omega = 1{\cdot}9$ rad/sec. (*a*) $\gamma = 1{\cdot}328$, counterclockwise rotation. (*b*) $\gamma = 2{\cdot}065$, clockwise rotation. Photograph was taken at 4·5 min in (*a*), 4·4 min in (*b*), after d.c. potential was applied across the electrode.